Downloaded from orbit.dtu.dk on: May 06, 2023

DTU Library

The nature of strong H I absorbers probed by cosmological simulations: satellite accretion and outflows

Rhodin, N. H. P.; Agertz, O.; Christensen, L.; Renaud, F.; Fynbo, J. P. U.

Published in:
Monthly Notices of the Royal Astronomical Society

Link to article, DOI:
10.1093/mnras/stz1479

Publication date:
2019

Document Version
Publisher's PDF, also known as Version of record

Link back to DTU Orbit

Citation (APA):
Rhodin, N. H. P., Agertz, O., Christensen, L., Renaud, F., & Fynbo, J. P. U. (2019). The nature of strong H I absorbers probed by cosmological simulations: satellite accretion and outflows. *Monthly Notices of the Royal Astronomical Society*, *488*(3), 3634-3645. https://doi.org/10.1093/mnras/stz1479

General rights
Copyright and moral rights for the publications made accessible in the public portal are retained by the authors and/or other copyright owners and it is a condition of accessing publications that users recognise and abide by the legal requirements associated with these rights.

- Users may download and print one copy of any publication from the public portal for the purpose of private study or research.
- You may not further distribute the material or use it for any profit-making activity or commercial gain
- You may freely distribute the URL identifying the publication in the public portal

If you believe that this document breaches copyright please contact us providing details, and we will remove access to the work immediately and investigate your claim.

Monthly Notices
of the
ROYAL ASTRONOMICAL SOCIETY

MNRAS **488,** 3634–3645 (2019)
Advance Access publication 2019 May 31

doi:10.1093/mnras/stz1479

The nature of strong H I absorbers probed by cosmological simulations: satellite accretion and outflows

N. H. P. Rhodin [1]★ O. Agertz [2] L. Christensen [1] F. Renaud [2] and J. P. U. Fynbo [3,4]

[1] *DARK, Niels Bohr Institute, University of Copenhagen, Lyngbyvej 2, DK-2100 Copenhagen Ø, Denmark*
[2] *Lund Observatory, Department of Astronomy and Theoretical Physics, Box 43, SE-221 00 Lund, Sweden*
[3] *Cosmic DAWN Center NBI/DTU-Space, University of Copenhagen, Lyngbyvej 2, DK-2100 Copenhagen Ø, Denmark*
[4] *Niels Bohr Institute, University of Copenhagen, Lyngbyvej 2, DK-2100 Copenhagen Ø, Denmark*

Accepted 2019 May 24. Received 2019 May 22; in original form 2019 January 29

ABSTRACT

We use cosmological hydrodynamic zoom simulations to study the neutral gas distribution in and around galaxies that gives rise to high column density H I Ly α absorption (damped Ly α systems (DLAs) and sub-DLAs) in background quasar spectra. Such simulations often sacrifice numerical resolution for volume that affects the lower density galaxy halo gas, and simulations have difficulties reproducing the span of projected separations (b) between absorbing clouds and their hosts. Our simulations produce (sub-)DLAs over the entire probed parameter space ($b \lesssim 50$ kpc and metallicity $-4 \lesssim$[M/H]$\lesssim 0.5$) at all redshifts ($z \sim 0.4 - 3.0$), enclosing spectroscopically confirmed absorber-galaxy pairs. Recovering (sub-)DLAs at $b \gtrsim 20 - 30$ kpc from a massive host galaxy requires high numerical resolution and efficient feedback, and we show that these lines-of-sight are associated with dwarf satellites in the main halo, stripped metal-rich gas, and outflows. H I disc- and halo gas significantly contributes to (sub-)DLAs around galaxies. At large redshifts the halo plays an increasingly important role, while at $0.4 < z < 1$ the disc and halo contribute with ∼60(80) and ∼40(20) per cent to column densities above the sub-DLA(DLA) lower limits. The distribution of b for sub-DLAs and DLAs overlap at $z \sim 2 - 3$, but evolves so that sub-DLAs on average are located at twice larger b by $z \sim 0.5$. A weak correlation suggests that sub-DLA covering fractions increase with stellar mass more rapidly than those of DLA. This can explain why sub-DLAs are preferentially selected in more massive galaxies in the low-z Universe.

Key words: galaxies: evolution – galaxies: formation – galaxies: haloes – galaxies: structure – intergalactic medium – quasars: absorption lines.

1 INTRODUCTION

The chance alignment of neutral gas clouds intervening the line of sight (LOS) towards background quasi-stellar objects (quasars) imprints characteristic absorption features in the quasar power-law continua. In neutral hydrogen (H I), the most H I-rich absorbers are the Damped Lyman α Absorbers (DLAs; $\log_{10}[N_{\rm HI}\,({\rm cm}^{-2})] \geq 20.3$; Wolfe et al. 1986) and the sub-DLAs ($19.0 \leq \log_{10}[N_{\rm HI}\,({\rm cm}^{-2})] < 20.3$; e.g. Péroux et al. 2003; Zafar, Popping & Péroux 2013). Unless otherwise specified, we refer to sub-DLAs and DLAs uniformly as strong H I absorbers. Both classes of absorbers are always accompanied by low-ionization metal line complexes (Prochaska et al. 2003; Noterdaeme et al. 2012; Rafelski et al. 2014) which suggests an association with a gaseous medium affected by chemical enrichment. Yet, the origin and nature of strong H I absorbers and their relation to galactic environments remains highly debated.

Absorption velocities and asymmetric line-profiles with leading edges (Prochaska & Wolfe 1997), as well as models of disc formation (Mo, Mao & White 1998), support the idea that DLAs preferentially probe rapidly rotating galaxy discs (Wolfe et al. 1986). However, using cosmological hydrodynamic simulations, Haehnelt, Steinmetz & Rauch (1998) demonstrated that the absorption kinematics could equally well be explained by irregular protogalactic clumps in dark matter haloes subject to a combination of rotation, random motions, gas flows, and mergers. A picture is emerging in which strong H I absorbers trace neutral gas on scales of tens of kpc in galaxies (Møller & Warren 1998; Christensen et al. 2007; Pontzen et al. 2008; Monier, Turnshek & Rao 2009; Fynbo et al. 2010, 2011; Meiring et al. 2011; Rao et al. 2011; Krogager et al. 2012; Péroux et al. 2012; Krogager et al. 2013; Fynbo et al. 2013b; Rahmati & Schaye 2014; Rahmani et al. 2016; Rhodin et al. 2018).

★ E-mail: henrikrhodin@dark-cosmology.dk

© 2019 The Author(s)
Published by Oxford University Press on behalf of the Royal Astronomical Society

Downloaded from https://academic.oup.com/mnras/article-abstract/488/3/3634/5509589 by DTU Library - Technical Information Center of Denmark user on 16 September 2019

A number of analytical models have been successful in reproducing observed bulk properties of DLAs (Fynbo et al. 2008; Krogager et al. 2017, from hereon the 'F08 + K17 model') (also Freudling et al., in preparation). By construction, these models depend on mean scaling relations of galaxies, and cannot capture processes related to galactic substructure or gas structures in the intergalactic medium. Large-scale cosmological hydrodynamic simulations have the potential to mitigate these shortcomings, and have been employed for over a decade (e.g. Nagamine et al. 2007; Pontzen et al. 2008; Fumagalli et al. 2011; Cen 2012; Rahmati et al. 2013; Faucher-Giguère et al. 2015; Liang, Kravtsov & Agertz 2016). Such simulations have been successful in reproducing a broad range of observables, including the H I column density distribution function and the distribution of DLA metallicities. However, such simulations struggle with reproducing the observed absorption kinematics (Pontzen et al. 2008; Bird et al. 2014, 2015); lack resolution to capture small-scale features of cold gas in haloes (Hummels et al. 2018; McCourt et al. 2018); and require very strong stellar feedback in order to produce cold gas at large impact parameters, destroying the star-forming gas discs in the process (Liang et al. 2016; Liang, Kravtsov & Agertz 2018).

Formal numerical convergence on the spatial scales advocated by McCourt et al. (2018) to resolve fragmented, cold gas clouds in the circumgalactic medium (CGM) on scales of $\sim 0.003 - 0.1$ pc is far beyond the current limits of cosmological simulations. However, recent work is capable of marginally resolving the total path-length of cold gas along the LOS, estimated to span a range of $0.1 - 100$ pc (McCourt et al. 2018). Such simulations are the so-called 'zoom-in simulations' which focus on the assembly of individual galaxies, and they provide a viable pathway towards understanding the distribution of strong H I absorbers, their significance as reservoirs of neutral gas, and their role in the cosmic baryon cycle. In particular, van de Voort et al. (2019) showed that already a uniform 1 kpc resolution to the virial radius significantly altered radial profiles of H I column densities, and lead to enhanced covering fractions of Lyman-Limit Systems ($\log_{10}[N_{\rm HI}\,({\rm cm}^{-2})] \geq 17.2$; Tytler 1982) within 150 kpc by a factor of two. Echoing the results of Hummels et al. (2018), Peeples et al. (2019) showed that whilst numerical resolution has a large impact on the physical state of the cold CGM gas and on its underlying kinematic structure, integrated quantities changed at $\lesssim$30 per cent level as the resolution was varied. These results suggest that resolving the CGM is crucial to our understanding of strong H I absorbers around galaxies.

The detection of strong H I absorbers at high impact parameters (b [kpc]) from their tentative host galaxies (see Christensen et al. 2019; Møller & Christensen 2019) provide clues to their nature and clustering. Fumagalli et al. (2011) suggest that cold streams accreting smoothly onto massive ($M_{\rm vir} = 10^{10} - 10^{12}$ M$_\odot$) galaxies contribute >50 per cent of the covering factor in strong H I absorption above $z = 4$; but that such stream's significance is replaced by contributions from galaxies, which dominate the cross-section below $z \sim 2$. Whereas cold stream accretion undeniably plays a vital role, Fumagalli et al. (2011)'s simulations severely underpredicted the equivalent widths of metal absorption lines, and their limited outflow- and feedback implementations renders conclusions biased to smooth, metal-poor, cold accretion. In addition, work using large-scale cosmological simulations have called into question the detection of these high-b absorbers, suggesting instead that observations suffer from a selection bias towards the most luminous (but unrelated) galaxy in the projected sky vicinity (Rahmati & Schaye 2014). Finally, we note that comparing impact parameters from simulations to those associated with confirmed galaxy counterparts of strong H I absorbers are difficult, as observational campaigns often pre-select on absorption-metallicity to ensure high detection rates. Given the uncertain numerical resolution requirements for capturing neutral gas in haloes, these issues warrants a revisit using higher resolution models with realistic feedback implementations.

In this work, we employ high resolution cosmological zoom simulations to build probability functions of the distribution of strong H I absorption in and around galaxies. These probability functions are matched to the most recent compilation of such spectroscopically confirmed absorber-galaxy pairs (Møller & Christensen 2019; Christensen et al. 2019, from hereon, the 'MC19' compilation) and the analytical F08 + K17 model, and are used to explore the physical origin of strong H I absorption. Throughout the analysis, we confine the comparison to a circular beam of 50 kpc radius, centred on the galaxy. This value is observationally motivated, and selected to enclose the current compilation of detections. The paper is organized as follows: Section 2 describes our simulations, with particular emphasis given to the feedback recipes and resolution, Section 3 presents our results, and Section 4 summarizes our conclusions.

2 SIMULATIONS

2.1 Simulation setup

We carry out a cosmological hydrodynamic + N-body zoom-in simulation of a Milky-Way-mass galaxy using the adaptive mesh refinement (AMR) code RAMSES (Teyssier 2002), assuming a flat Λ-cold dark matter cosmology with $H_0 = 70.2\,{\rm km\,s^{-1}\,Mpc^{-1}}$, $\Omega_{\rm m} = 0.272$, $\Omega_\Lambda = 0.728$, and $\Omega_{\rm b} = 0.045$. From a dark matter-only simulation, with a simulation cube of size $L_{\rm box} = 85$ Mpc at $z = 0$, a halo of $R_{200,{\rm m}} = 334$ kpc (radius within which the mass density is 200 times the mean matter density) and $M_{200,{\rm m}} = 1.3 \times 10^{12}$ M$_\odot$ was selected for resimulation at high resolution. Particles within $3R_{200,{\rm m}}$ at $z = 0$ were traced back to $z = 100$, and the Lagrangian region they defined was regenerated at high resolution, still embedded within the full lower resolution volume, using the MUSIC code (Hahn & Abel 2011). The simulation was then run to $z = 0$, with outputs every $\Delta a = 0.01$. These are the same initial conditions as the 'm12i' halo from Hopkins et al. (2014) and Wetzel et al. (2016), drawn from the volume used in the AGORA galaxy formation comparison project (Kim, Abel & Agertz 2014; Kim et al. 2016).

The dark matter particle mass in the high resolution region is $m_{\rm dm} = 3.5 \times 10^4$ M$_\odot$, with a gas mass resolution of 7070 M$_\odot$. Star formation is sampled using 10^4 M$_\odot$ particles, with stellar evolution reducing this by up to 50 per cent (see below). The adaptive mesh is allowed to refine if a cell contains more than eight dark matter particles. This allows the local force softening to closely match the local mean interparticle separation, which suppresses discreteness effects (e.g. Romeo et al. 2008). A similar criterion is employed for the baryonic component, where the maximum refinement level is set to allow for a mean constant physical resolution of $\sim$20 pc in the dense interstellar medium. As such, this simulation is a significant improvement over previous cosmological zoom simulation used to study cold gas in and around galaxies (e.g. Liang et al. 2016).

The adopted star formation and feedback physics is presented in Agertz et al. (2013) and Agertz & Kravtsov (2015, 2016). Briefly, star formation is treated as a Poisson process occurring on a cell-by-cell basis according to the star formation law,

$$\dot{\rho}_\star = \epsilon_{\rm ff} \frac{\rho_{\rm g}}{t_{\rm ff}}, \quad (1)$$

Downloaded from https://academic.oup.com/mnras/article-abstract/488/3/3634/5509589 by DTU Library - Technical Information Center of Denmark user on 16 September 2019

where $\dot{\rho}_\star$ is the star formation rate density, ρ_g the gas density, $t_{ff} = \sqrt{3\pi/32G\rho_g}$ is the local free-fall time, and ϵ_{ff} is the local star formation efficiency per free-fall time of gas in the cell. The efficiency is computed following the relation from Padoan, Haugbølle & Nordlund (2012), derived from simulations of star formation in magnetized supersonic turbulence.[1]

Each formed star particle is treated as a single-age stellar population with a Chabrier (2003) initial mass function. We account for injection of energy, momentum, mass, and heavy elements over time from Type II and Type Ia supernovae (SNe), stellar winds, and radiation pressure (allowing for both single scattering and multiple scattering events on dust) on the surrounding gas. Each mechanism depends on the stellar age, mass, and gas/stellar metallicity (through the metallicity-dependent age–mass relation of Raiteri, Villata & Navarro 1996), calibrated on the stellar evolution code STARBURST99 (Leitherer et al. 1999).

Furthermore, to accurately account for SN feedback we adopt the SN momentum injection model recently suggested by Kim & Ostriker (2015, see also Martizzi, Faucher-Giguère & Quataert 2015). A SN explosion is considered resolved when its cooling radius[2] is captured by at least six grid cells. In this case the explosion is initialized in the energy conserving phase by injecting the relevant energy (10^{51} erg per SN) into the nearest grid cell. If this criterion is not fulfilled, the SN is initialized in its momentum conserving phase, i.e. the total momentum generated during the energy conserving Sedov–Taylor phase is injected into the cells surrounding a star particle. It can be shown (e.g. Blondin et al. 1998; Kim & Ostriker 2015) that at this time, the momentum of the expanding shell is approximately $4 \times 10^5 (E_{SN}/10^{51}\,\mathrm{erg})^{16/17} (n/1\,\mathrm{cm^{-3}})^{-2/17}\,\mathrm{M_\odot\,km\,s^{-1}}$.

We track iron (Fe) and oxygen (O) abundances separately, and advect them as passive scalars. When computing the gas cooling rate, which is a function of total metallicity, we construct a total metal mass as

$$M_Z = 2.09 M_O + 1.06 M_{Fe} \quad (2)$$

according to the mixture of alpha (C, N, O, Ne, Mg, Si, S) and iron (Fe, Ni) group elements relevant for the sun (Asplund et al. 2009). The code accounts for metallicity-dependent cooling by using tabulated cooling functions of Sutherland & Dopita (1993) for gas temperatures of $10^{4-8.5}$ K, and rates from Rosen & Bregman (1995) for cooling down to lower temperatures. Heating from the ultraviolet background radiation is accounted for by using the model of Haardt & Madau (1996), assuming a reionization redshift of $z = 8.5$. Self-shielding is modelled following the model of Aubert & Teyssier (2010). Finally, we follow Agertz, Teyssier & Moore (2009) and adopt an initial metallicity of $Z = 10^{-3}\,Z_\odot$ in the high-resolution zoom-in region in order to account for enrichment from unresolved population III star formation (e.g. Wise et al. 2012).

2.2 Model verification and analysis

By accounting for the above stellar feedback budget, Agertz & Kravtsov (2015, 2016) simulated the cosmological assembly of Milky-Way-mass galaxies, demonstrating that it led to a realistic late-type galaxy matching observed properties such as disc size, the presence of a thin and thick stellar disc, stellar and gas surface density profiles, the Kennicutt–Schmidt relation, the stellar mass–gas metallicity relation (and its evolution), and a specific angular momentum typical of spiral galaxies of the Milky Way mass (stellar mass of $\approx 5 \times 10^{10}\,\mathrm{M_\odot}$).

The simulation considered in this work reaches a significantly higher mass and spatial resolution, and matches the above-mentioned observational relations (to be presented in Agertz et al. in preparation). Furthermore, we find that H I column density distributions, $f(N_{HI})$, at all redshifts feature a turnover at column densities $N_{HI} \sim 10^{21}\,\mathrm{cm^{-2}}$, as observed both at high and low redshifts (Zwaan et al. 2005; Noterdaeme et al. 2009), and in the ISM of individual local galaxies (see analysis by Erkal, Gnedin & Kravtsov 2012). Our simulation does therefore not suffer from an excess of high column density H I ($N_{HI} \gg 10^{21}\,\mathrm{cm^{-2}}$) in the inner few kpc of galaxies, as found by Erkal et al. (2012) in their high resolution simulations with inefficient stellar feedback.[3] As such, our zoom simulation is a relevant platform for studying the nature of DLA and sub-DLA LOS in and around massive disc galaxies.

Using the dark matter halo finder HOP (Eisenstein & Hut 1998), we identify all dark matter haloes[4] within the simulated high resolution volume, in all simulation snapshots (see Section 2.1). For each halo, we generate 2D maps of N_{HI} and metallicity ([M/H]). We obtain H I from the neutral gas density in each cell by correcting for its molecular hydrogen content using the model by Krumholz, McKee & Tumlinson (2008, 2009), as implemented in Agertz & Kravtsov (2015).

All maps cover an area of $200 \times 200\,\mathrm{kpc^2}$, and are centred on the dark matter and stars using a shrinking sphere algorithm (Power et al. 2003). The pixels have the same sizes as the finest cell sizes available in the simulation at the given snapshot, typically $\Delta x \sim 20$ pc. In each pixel, the quantities have been computed as

$$N_{HI} = \sum_i n_{HI,i} \Delta x_i \quad (3)$$

and

$$[\mathrm{M/H}] = \frac{\sum_i n_{HI,i} [\mathrm{M/H}]_i}{\sum_i n_{HI,i}}, \quad (4)$$

where the sum runs over all cells along a given pixel LOS along the simulation volume (with a 200 kpc depth), $n_{HI,i}$ is the local cell density of neutral hydrogen, $[\mathrm{M/H}]_i$ the local cell gas metallicity, and Δx_i the size of a cell. For each snapshot, we compute maps from the three Cartesian directions. In subsequent sections we will present results both for single snapshots and directions to illustrate our findings, as well as results averaged over all analysed directions and different redshift ranges. Finally, quoted impact parameters b are defined as the projected distance from the centre of the main galaxy to a point of interest.

Numerical studies of DLAs have generally focused on large simulations volumes in order to capture a statistical sample of galaxies, at the sacrifice of numerical resolution (see Section 1).

[1] $\epsilon_{ff} = 0.5 \exp(-1.6 t_{ff}/t_{dyn})$, where the dynamical time is $t_{dyn} = L/2\sigma$, and σ is the local velocity dispersion computed using neighbouring gas cells over a region of size $L = 3$ grid cells per spatial dimension.

[2] The cooling radius in gas of density n and metallicity Z scales as $r \approx 30 (n/1\,\mathrm{cm^3})^{-0.43} (Z/Z_\odot + 0.01)^{-0.18}$ pc for a supernova explosion with energy $E_{SN} = 10^{51}$ erg (e.g. Cioffi, McKee & Bertschinger 1988; Thornton et al. 1998).

[3] Using simulations at lower numerical resolution, Altay et al. (2011) found that the H I–H_2 transition was sufficient to explain the observed turnover, in contrast to Erkal et al. (2012) (see also Altay et al. 2013) who argued that establishing a realistic star formation-feedback cycle is crucial for explaining the column density distribution of DLAs.

[4] Substructures are not robustly identified using HOP, but as we are mainly interested in central galaxies, this is no issue.

Downloaded from https://academic.oup.com/mnras/article-abstract/488/3/3634/5509589 by DTU Library - Technical Information Center of Denmark user on 16 September 2019

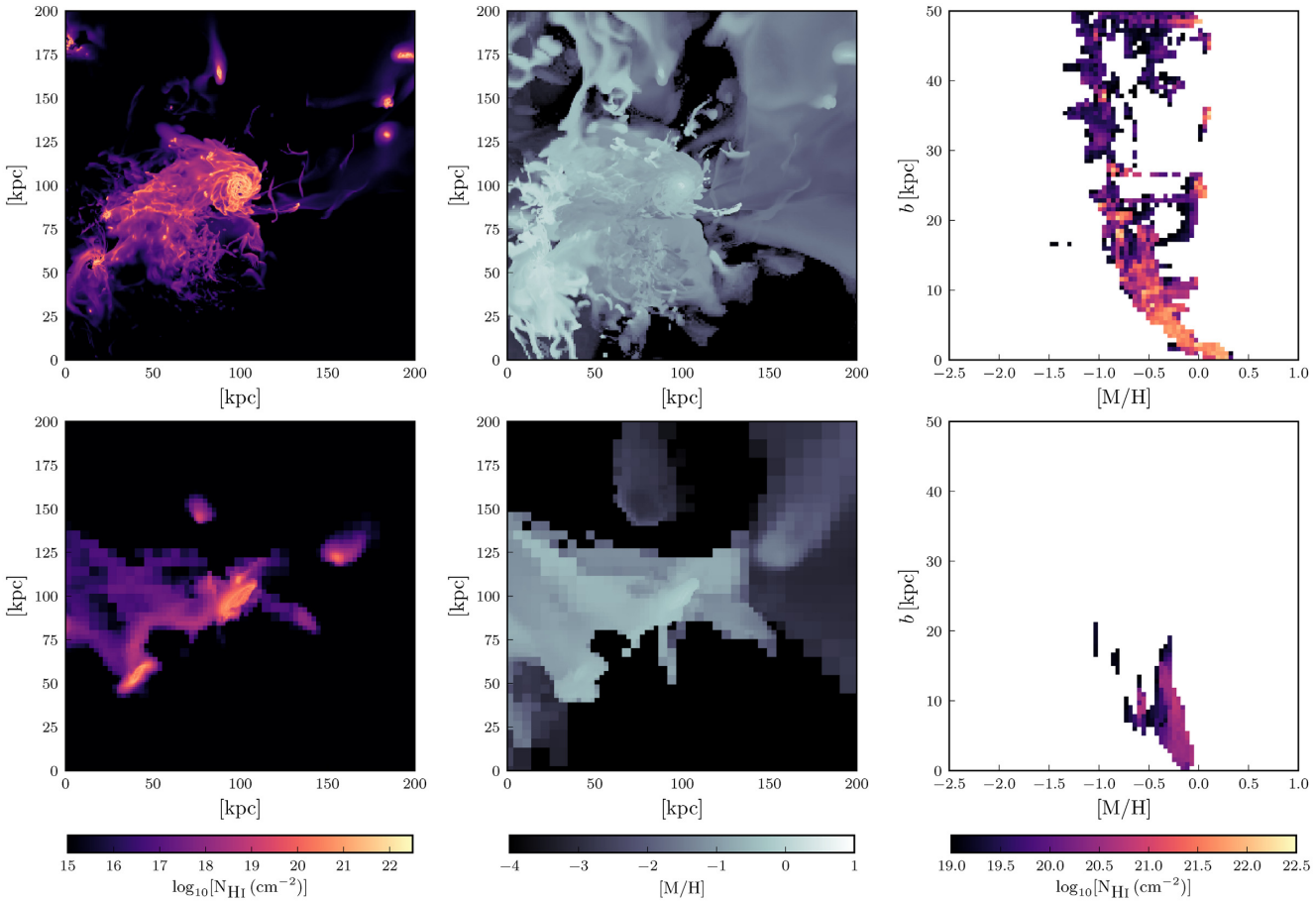

Figure 1. H I column density projection (left-hand panel), neutral gas metallicity (centre), and projected separation as a function of metallicity for gas above the lower sub-DLA column density limit (right-hand panel). The top row features the simulated central galaxy at fiducial resolution (see Section 2.1), with the bottom row presenting a low resolution version, comparable to the typical numerical resolution achieved in large volume cosmological simulations discussed in Section 2.2. The enhanced resolution increases the strong H I ($\log_{10}[N_{\rm HI}\,({\rm cm}^{-2})] > 19$) covering fractions at large projected radii, and reveals a complex, turbulent disc–halo interface with small-scale H I structures.

Indeed, modern cosmological simulations of galaxy formation in domains with sizes of over tens of Mpc, aimed at reproducing the stellar luminosity function, e.g. EAGLE (Schaye et al. 2015) and Illustris (Vogelsberger et al. 2014), have been restricted to spatial resolutions of $\sim 0.5 - 1$ kpc. In contrast, we are here interested in a specific set of observations relating DLAs and sub-DLAs, at impact parameters up to $b \sim 50$ kpc, to confirmed host galaxies, here predominantly massive and star forming (see Section 3.1), making a comparison to high resolution zoom simulations more appropriate.

The importance of high numerical resolution is illustrated in Fig. 1. The top row shows $N_{\rm HI}$ and [M/H] maps, as well as b versus [M/H], at $z = 1$ for the most massive galaxy in our zoom region ($M_\star \sim 5 \times 10^{10}\,{\rm M}_\odot$). The bottom row shows the same quantities, but for the simulation run at 32 times lower spatial resolution ($\Delta x \sim 640$ pc), and dark matter particle masses of $1.4 \times 10^6\,{\rm M}_\odot$, compatible with the aforementioned large volume simulations. While the low-resolution simulation also leads to an extended disc, with a similar stellar mass at $z = 0$ (made possible by the stellar feedback driven galactic outflows), the lack of detail in the CGM compared to the fiducial high resolution model is striking. In this work, we have not performed convergence tests. However, the cold, dense gas is not artificial, but an emergent feature at the fiducial resolution of our simulations. This gas will not disappear by further enhancing resolution. On the contrary, it will reveal more cold gas at large galactocentric distances until formal convergence is reached (Hummels et al. 2018; McCourt et al. 2018), and our qualitative results on the cold gas contents can therefore conservatively be treated as lower limits.

The fiducial model resolves a greater number of low mass satellites, all found to contribute to DLA and sub-DLA detections (see also Section 3.2). In addition, galaxy interactions, inflows, and feedback driven outflows create complex gas structures with large covering fractions (see Sections 3.2 and 3.4). A significant fraction of these gas structures shows high levels of metal-enrichment for which feedback and satellite accretion is key; most prominently observed as potential strong H I detections at $b > 20$ kpc in the b −[M/H] plane (Section 3.1). All of the above are crucial in order to interpret the observations presented in the next following analysis.

3 RESULTS

3.1 Comparing simulations to analytical models

The simple analytical F08 + K17 model was built to capture very basic statistical properties of DLAs and their galaxy counterparts such as relations between impact parameter, metallicity, and lu-

Downloaded from https://academic.oup.com/mnras/article-abstract/488/3/3634/5509589 by DTU Library - Technical Information Center of Denmark user on 16 September 2019

minosity. The model does not include physical properties such as the role of environment, inflows and outflows, and does not account for radiative transfer effects and density gradients. Despite its simplicity, it is able to reconcile the metallicity distributions of gamma-ray bursts, quasar DLAs, and Lyman-break galaxies (LBGs) – suggesting that these objects are selections of the same underlying galaxy population (Fynbo et al. 2008). When combined with the Krogager et al. (2017) recipe for UV luminosity and expected SFR, the model accurately predicts the fraction of identified counterparts in surveys of absorption-selected galaxies that utilize different observing strategies.

The model describes DLAs as resulting from random LOS through infinitely thin, inclined slabs of 'DLA-gas' smeared across a disc-like geometry, calibrated to ensure that the cross-section matches the observed line density of DLAs at $z = 3$ (Prochaska, Herbert-Fort & Wolfe 2005). It combines a $z \sim 3$ UV luminosity function (Reddy et al. 2008); a $z \sim 3$ metallicity–luminosity relation (Pettini et al. 2001); a $z \sim 0$ local Holmberg relation to describe the size of the H I disc as a function of the galaxy luminosity (following Wolfe et al. 1986 and originally derived from local discs in the Virgo- and Hercules clusters by Holmberg et al. 1975 and Peterson, Strom & Strom 1979); and a prescription for the metallicity gradient following Boissier & Prantzos (2001). In light of its success, with our simulations we now ask if the assumed scaling relations are reproduced in the simulations and if so at which redshifts.

To answer this, we use HOP to identify the most massive dark matter halo, and follow its evolution in redshift from $z = 3$ to $z = 0.4$. This halo grows in stellar mass from $9.6 \leq \log_{10}[M_\star\,(\mathrm{M}_\odot)] \leq 10.8$, which matches the LBG population stellar mass distribution $\log_{10}[M_\star\,(\mathrm{M}_\odot)] = 9.87 \pm 0.53$ (Reddy & Steidel 2009) from whose luminosity function the F08 + K17 model was constructed. We compute b (kpc), [M/H], and $\log_{10}[N_{\mathrm{H\,I}}\,(\mathrm{cm}^{-2})]$ at each redshift and along each side of the simulation-box using the method described in Section 2.2. Binning in redshift intervals, we calculate the angle-averaged detection fractions ($f_{\mathrm{detections}}$) at each locus. The results are presented in Fig. 2 and consists of probability functions in the b (kpc) − [M/H] – and the b (kpc) − $\log_{10}[N_{\mathrm{H\,I}}\,(\mathrm{cm}^{-2})]$ parameter space, with $f_{\mathrm{detections}}$ normalized for each panel. We show these results together with predictions from the F08 + K17 model (with the mean relation (black solid), the 1σ-, 2σ-, and 3σ intrinsic dispersion (grey solid) contours and model envelope (grey dashed line)), and the MC19 compilation for a sequence of redshifts (columns). It is worth noting that galaxies above $b \gtrsim 30$ kpc from quasar LOSs have historically been considered unlikely counterparts to strong H I absorbers. Therefore, the accumulated observational data may by selection only probe the lower range of possible impact parameters. Row one shows a simulation snapshot centred on the galaxy; rows two- and three show the space spanned by b (kpc) − [M/H] with a cut on the column density at the sub-DLA and at the DLA lower limits, respectively; and row four spans the b (kpc) − $\log_{10}[N_{\mathrm{H\,I}}\,(\mathrm{cm}^{-2})]$ parameter space.

Fig. 2 reveals significant detection probabilities of LOS above the DLA column density threshold extending to impact parameters of 50 kpc from the host centre, across all redshifts. It can also be seen that the distribution clearly changes with redshift. Qualitatively, this can be understood as follows: at higher redshifts the higher density of galaxies inherent to hierarchical structure formation give rise to higher merger frequencies, and more tidal interactions and turbulent disturbances. At $z > 2$, this inhibits gas from settling into coherent and long-lived structures such as extended H I discs. We therefore see $f_{\mathrm{detections}}$ across a broad range of gridpoints in the b (kpc) − [M/H] – and the b (kpc) − $\log_{10}[N_{\mathrm{H\,I}}\,(\mathrm{cm}^{-2})]$ parameter spaces alike. This is particularly clear in the highest redshift panel ($z = 2 - 3$, Fig. 2 bottom left-hand panel), for which our simulations generate detections across the whole parameter space.

Towards progressively lower redshift, merger rates and densities drop, and the H I gas is allowed to settle. This includes the formation of an H I disc that encodes information on a metallicity-gradient, most prominently observed as the diagonal stripe of high detection probability (Fig. 2 third row, rightmost panel, but see also Section 3.2 for a direct observation of the disc in this parameter space). In the same row, we also find a region of diffuse (lower detection probability per unit gridpoint) $f_{\mathrm{detections}}$ but extending to large impact parameters. This is indicative of a significant contribution from the CGM and the extended halo to the DLA cross-section (see Sections 3.2 and 3.3).

In Table 1 we quantify the agreement between the F08 + K17 model and our simulation by calculating the summed detection-fraction enclosed within the 1σ-, 2σ-, and 3σ limits. The DLA LOS detection fractions in simulations converge to model predictions towards progressively lower redshifts, reaching a good agreement at $z \sim 0.8$. This may be related to the evolution and stability of the H I disc, in which case the model assumption of a geometrically thin, but optically thick slab of gas above the DLA column density limit is valid below $z \sim 0.8$ (see Section 3.2). If true, this can explain the statistical convergence of observational data, model-confidence regions, and simulation results toward low-redshift when an H I disc is present.

Relaxing the threshold on the column-density to include detection-fractions from sub-DLA LOS in b (kpc) − [M/H] (Fig. 2, second row), we find that $f_{\mathrm{detections}}$ becomes less concentrated and covers a larger region in the parameter-space at all redshifts. Phenomenologically, this suggests that sub-DLA LOS fill the void between islands of DLA-$f_{\mathrm{detections}}$, and could be related to a density gradient such that sub-DLAs on average trace lower density gas. We pursue this by separating the galaxy into a halo and a disc (Section 3.2) and quantify statistical differences between the average DLA and sub-DLA LOS in Sections 3.3 and 3.4.

In Table 2 we demonstrate how the inclusion of sub-DLA column densities affects the match between simulation $f_{\mathrm{detections}}$ and the analytical disc model predictions. We find that such an inclusion results in a worse match at all redshifts. This most probably reflects the underlying Holmberg relation in the construction of the model, which works well down to the lower limit of DLA column densities. Indeed, this statistical discrepancy also matches the observational results of Rhodin et al. (2018), who found an excess of sub-DLAs beyond the predicted 1σ model region. We therefore conclude that in order to match simulations and observational data below the formal DLA limit, the analytical disc model must be amended or expanded.

3.2 The fraction of DLA/sub-DLA systems in discs and haloes

The relative contributions of interstellar ('disc') and circumgalactic ('halo') gas to DLA and sub-DLA detections are not yet known. Despite employing an infinitely thin circular disc to define a geometry on which to distribute the DLA cross-section, the F08 + K17 model does not claim to describe galactic H I discs. In simulations, such a separation is complicated as these gaseous components are ill-defined, especially for the earliest stages of disc formation. This is especially true for gas in the interface between the disc and the halo, related to accretion and outflows. The results below should hence be treated as indicative.

Downloaded from https://academic.oup.com/mnras/article-abstract/488/3/3634/5509589 by DTU Library - Technical Information Center of Denmark user on 16 September 2019

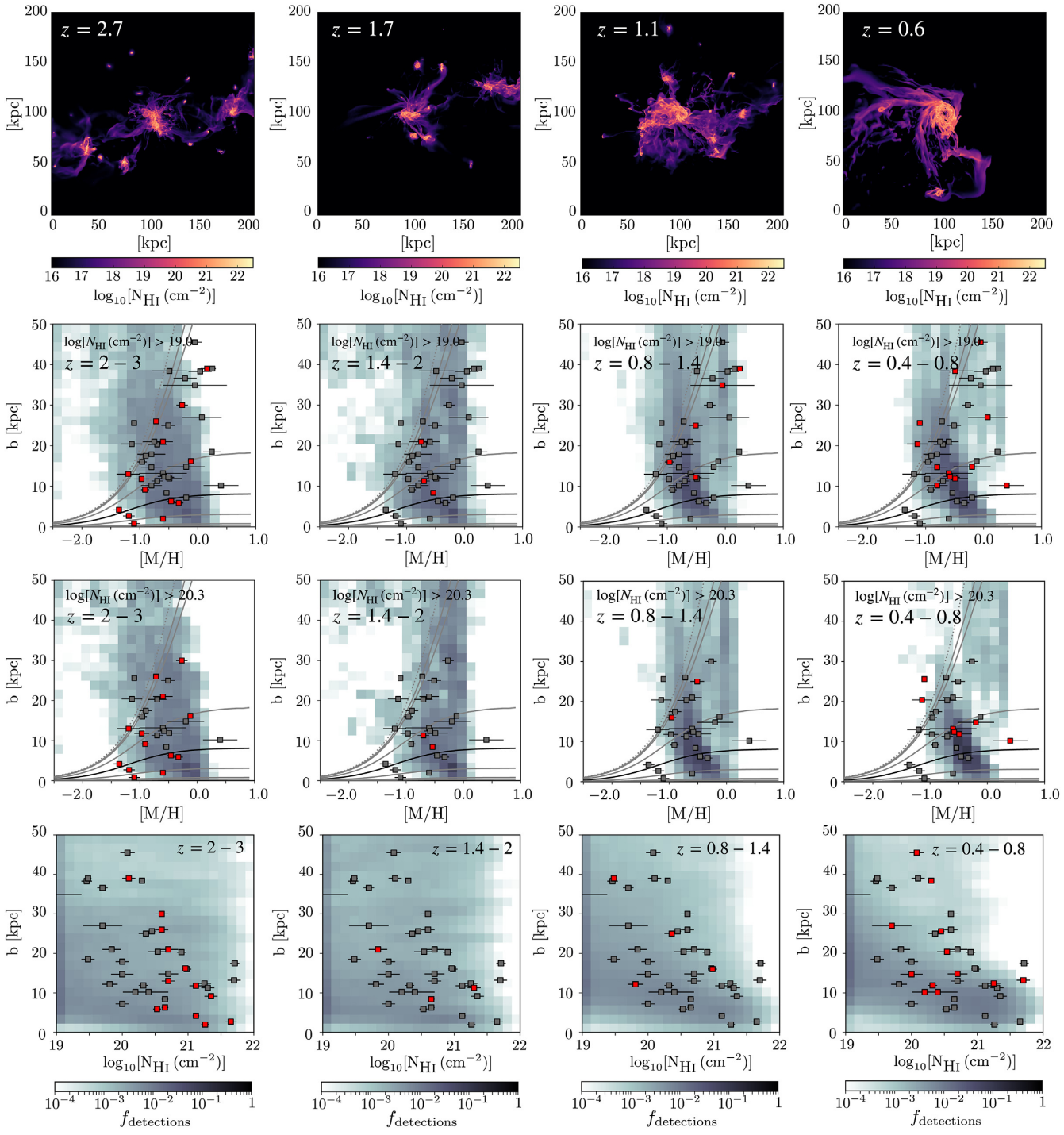

Figure 2. First row: H I column-density projections of the simulated central galaxy. Second row: Angle-averaged detection fractions of sightlines above the sub-DLA column-density limit ($\log_{10}[N_{\rm HI}\,({\rm cm}^{-2})] = 19$) within an observationally motivated beam of 50 kpc radius (in projected separation). Third row: Same as second row, cut at the DLA column-density limit ($\log_{10}[N_{\rm HI}\,({\rm cm}^{-2})] = 20.3$). Fourth row: Angle-averaged detection fractions in the space spanned by projected distance and H I column density. Image columns depict the redshift-evolution in the relations, moving from high (left-hand column) to progressively lower redshifts. The MC19 compilation of observations has been overplotted as individual data points. The data have been filtered to the column-density threshold of the row, and are colour-coded to depict the data in the redshift-range of the image column in red. In rows two and three, we have overplotted the mean (black solid), 1σ-, 2σ-, and 3σ contours (grey solid) and the model envelope (grey dashed line) of the analytical F08 + K17 model.

We adopt the following simple approach for separating neutral disc gas from halo gas, and apply it to our most massive galaxy in the zoom-in region. For each simulation snapshot, the angular momentum vector is computed for all baryons residing within $3r_{1/2}$ of the central galaxy, where $r_{1/2}$ is the (baryonic) half-mass radius. This defines a disc plane, for which we compute the density profile $n(r)$ of neutral *gas*, where r is the spherical radius. Such profiles are nearly exponential, with a fall-off below $n(r) \sim 10^{-2}\,{\rm cm}^{-3}$ due

Downloaded from https://academic.oup.com/mnras/article-abstract/488/3/3634/5509589 by DTU Library - Technical Information Center of Denmark user on 16 September 2019

Table 1. Simulation-based detection fractions of DLA-LOS enclosed within the F08 + K17 model 1σ-, 2σ-, and 3σ confidence regions.

Redshift range	1σ (0.68)	2σ (0.95)	3σ (0.99)
3.0 − 2.0	0.41	0.74	0.77
2.0 − 1.4	0.41	0.81	0.85
1.4 − 0.8	0.58	0.89	0.91
0.8 − 0.4	0.78	0.97	0.98

Table 2. Same as Table 1, but including sub-DLA LOS.

Redshift range	1σ (0.68)	2σ (0.95)	3σ (0.99)
3.0 − 2.0	0.41	0.70	0.74
2.0 − 1.4	0.39	0.76	0.81
1.4 − 0.8	0.42	0.77	0.81
0.8 − 0.4	0.54	0.84	0.87

to the inability of gas to self-shield against the background UV field (also found in the radiative transfer calculations by Aubert & Teyssier 2010). We define the size of the disc to be the radius $r_{\rm d}$ where $n(r)$ falls below $n = 10^{-3}$ cm^{-3}, but note that our conclusions are not very sensitive to cut-off densities in the range to $n = 10^{-4} - 10^{-2}$ cm^{-3}. At $z < 1$, $r_{\rm d}$ fall in the range $\sim$15 − 30 kpc. For each simulation snapshot, all neutral gas inside of the cylindrical radius $r_{\rm d}$ and below an altitude above the disc plane of $h = 8$ kpc is defined as 'disc', and the gas outside of this domain is defined as 'halo'.

At high redshifts ($z \gtrsim 1 - 2$), mergers and galaxy interactions yield mostly transient discs – if at all. To allow for a cleaner disc–halo separation, we restrict our analysis to $z < 1$, and in order to convey that a robust (as opposed to a transient) disc is identified, we stack the results between $z = 0.4$ and 1. In this way, we ensure that our methodology is not biased to the conditions of a single snapshot. The results of the component separation are shown in Fig. 3, for which the top row displays an H I column density map of the galaxy (left-hand panel), the H I disc (centre), and halo (right-hand) at $z = 0.6$. Row two and three display the stacked detection fractions in the b −[M/H] plane, with lower column-density thresholds set to sub-DLA and DLA limits, respectively. Our simple approach allows a clear disc component to be extracted, with the residual halo gas containing satellites, stripped filamentary gas, and gas at smaller impact parameters residing just outside, but soon to be accreted onto, the disc.

The disc component is visually distinct in the b −[M/H] relation, both for DLA LOS alone, and when sub-DLA LOS are included, and extends all the way to the 3σ confidence relation of the analytical F08 + K17 model. In fact, 99.6 per cent (88 per cent) of all simulated DLA sightlines lie within the $2(1)\sigma$ relation, indicating that the F08 + K17 model does not necessarily represent the physical nature of turbulent discs, but illustrates why this model has been highly successful in capturing observational properties of DLAs (Krogager et al. 2017). For the above disc definition, $\sim$40 per cent (60 per cent) of LOS with $\log_{10}[N_{\rm HI}\,({\rm cm}^{-2})] > 19$ intersect 'halo' ('disc') gas, and $\sim$20 per cent (80 per cent) for $\log_{10}[N_{\rm HI}\,({\rm cm}^{-2})] > 20.3$. By allowing for a disc definition with $h = 4$ kpc, rather than 8 kpc, we find identical results, indicating that our results are robust to reasonable parameter changes. In summary, our experiments illustrate that for the extended disc galaxy of the type analysed here, compatible with $L_\star$ galaxies ($M_\star \sim$ few $\times\, 10^{10}$ M$_\odot$) and for $z < 1$, DLAs predominantly originate in extended H I discs, but with halo gas playing a role at all impact parameters – especially at high impact parameters and in the sub-DLA regime.

Both simulations and observations indicate a significant amount of metal-rich DLA/sub-DLA LOS at high impact parameters ($b \gtrsim 25$ kpc). From the simulated component separation, it is clear that most of the gas contributing to these LOS is of halo origin. We interpret this as a clear sign of metal-rich gas stripped from dwarf satellites, as the shallow potential wells in these galaxies allow for efficient unbinding of enriched gas via outflows, ram pressure, and tidal stripping. This is supported by the metallicity map in Fig. 1 which shows high metallicity gas extending from the satellites; and visually by the presence of satellites and stripped tidal tails in the halo component of the main galaxy in Fig. 3. We caution that this is a qualitative assessment. Rigorously tracing the precise origins of metals and mixing of gas requires particle tracing methods (e.g. Genel et al. 2013; Cadiou, Dubois & Pichon 2019). Such methods will help us understand flows through the CGM and the disc–halo interface, and to quantify the contribution from satellites, which we leave for future work.

3.3 A redshift evolution in the mean impact parameters

The results of Section 3.1 suggest that there is a redshift evolution in the internal distribution of sub-DLA and DLA LOS through a galaxy, and that this evolution may be different for sub-DLAs and DLAs. We know from observations that strong H I absorbers follow a column-density-dependent distribution of impact parameters (Christensen et al. 2007; Monier et al. 2009; Fynbo et al. 2010, 2011; Meiring et al. 2011; Rao et al. 2011; Rahmani et al. 2016). Marginalizing over redshifts, these observations state that DLA LOS are found systematically closer to their host galaxy than sub-DLA LOS by a factor of $\sim$2 (Rao et al. 2011; Rhodin et al. 2018). Likewise, investigations of the ΔV_{90} − $[{\rm M/H}]_{\rm abs}$ relation (e.g. Ledoux et al. 2006; Møller et al. 2013; Neeleman et al. 2013) have shown that DLAs have smaller mean velocity widths and lower metallicities than sub-DLAs (e.g. Som et al. 2015). Taken together, these observations suggest that the two classes of absorbers on average trace different parts of their hosts.

We now explore whether we can quantify such average differences. The simplest nonparametric statistic to quantify the difference is the mean impact parameters of sub-DLA and DLA LOS. From here onwards, these will be referred to as $\langle\, b_{\rm sub\text{-}DLA}\rangle$ and $\langle\, b_{\rm DLA}\rangle$, respectively. These quantities are particularly interesting from an observational point of view, as impact parameters are amongst the simplest observables and readily available for 43 absorber-galaxy pairs in the MC19 compilation. In addition, the analysis presented in Section 3.1 suggest that DLA LOS can be found at large impact parameters with significant probabilities.

We first calculate $\langle\, b_{\rm sub\text{-}DLA}\rangle$ and $\langle\, b_{\rm DLA}\rangle$. To ensure that the galaxy analysed in previous sections is not an outlier, we allow HOP (see Section 2.2) to identify the seven most massive haloes. This allows us to cover diverse galaxy environments, a stellar mass range of $6.7 < \log_{10}[M_\star\,({\rm M}_\odot)] < 10.8$ which covers most observations, and to span a redshift range $0.4 < z < 3.0$. Using the information on $\langle\, b_{\rm sub\text{-}DLA}\rangle$ and $\langle\, b_{\rm DLA}\rangle$ together with the associated redshift and stellar mass from the three Cartesian directions and for each of the haloes, we present the results in Fig. 4. The top panel displays the individual data of $\langle\, b_{\rm sub\text{-}DLA}\rangle$ (orange) and $\langle\, b_{\rm DLA}\rangle$ (grey) together with their binned-mean relations in the respective colours, as a function of redshift. The results indicate a co-evolution in mean DLA- and sub-DLA impact parameters towards progressively smaller values with time. However, perhaps the most striking feature is the large scatter

Downloaded from https://academic.oup.com/mnras/article-abstract/488/3/3634/5509589 by DTU Library - Technical Information Center of Denmark user on 16 September 2019

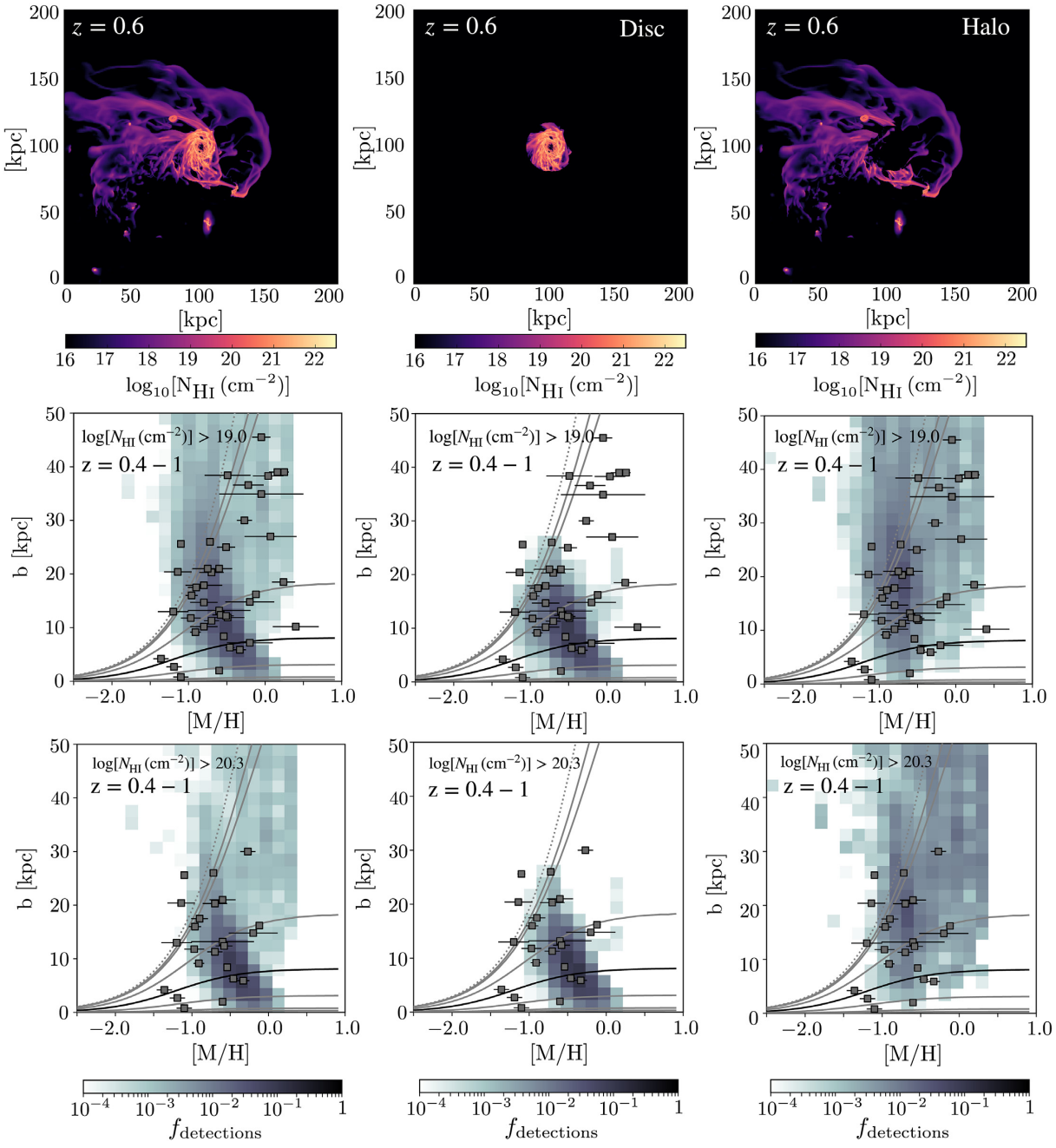

Figure 3. H I column density projection of the central galaxy (top) split into three panels depicting the total H I gas projection (left-hand panel), the disc component (centre), and halo (right-hand panel). The bottom panels display the associated distributions of detection-fractions in the $b-$ [M/H] plane, with cuts at the sub-DLA and DLA threshold, respectively. The integral of detection-fractions in a panel measures the contribution of that structure to the total number of LOS producing strong H I absorption above the associated column-density threshold.

in the mean values at any redshift. The scatter is set from the range of galaxy-sizes spanned by the seven haloes, and the effect of a fixed 50 kpc beam. To cancel the size-dependence and enhance any differential change in the mean impact parameters with redshift, in the bottom panel, we therefore proceed to plot the ratio of the means; $\langle\, b_{\rm DLA}\rangle/\langle\, b_{\rm sub\text{-}DLA}\rangle$. A horizontal line implies a scale-free fraction, which at unity translates to identical mean impact parameters for sub-DLA and DLA LOS. For reference, we display such a 1: 1 relation as a red dashed line.

To ensure that any correlation in $\langle\, b_{\rm DLA}\rangle/\langle\, b_{\rm sub\text{-}DLA}\rangle$ with redshift is indeed real, and not a consequence of an underlying correlation with stellar mass, we calculate the Pearson (PC) coefficient, the Spearman rank-order correlation (SC) coefficient, and their associated null-hypothesis's p-values. Expressed Test (parameter1, parameter2) = [coefficient, $p-$ value] we find PC($\langle\, b_{\rm DLA}\rangle/\langle\, b_{\rm sub\text{-}DLA}\rangle$, $\log_{10}[M_\star\,(\mathrm{M}_\odot)]$) = [0.073, $\sim 10^{-2}$] and SC($\langle\, b_{\rm DLA}\rangle/\langle\, b_{\rm sub\text{-}DLA}\rangle$, $\log_{10}[M_\star\,(\mathrm{M}_\odot)]$) = [0.144, $\sim 10^{-5}$], whereas significantly higher correlation coefficients are identified for PC($\langle\, b_{\rm DLA}\rangle/\langle\, b_{\rm sub\text{-}DLA}\rangle$, z) = [0.396, $\sim 10^{-31}$], SC($\langle\, b_{\rm DLA}\rangle/\langle\, b_{\rm sub\text{-}DLA}\rangle$, z) = [0.399, $\sim 10^{-32}$]. With consistent results from a Pearson and a Spearman test, both strongly suggesting that redshift is indeed the primary driver in the impact param-

Downloaded from https://academic.oup.com/mnras/article-abstract/488/3/3634/5509589 by DTU Library - Technical Information Center of Denmark user on 16 September 2019

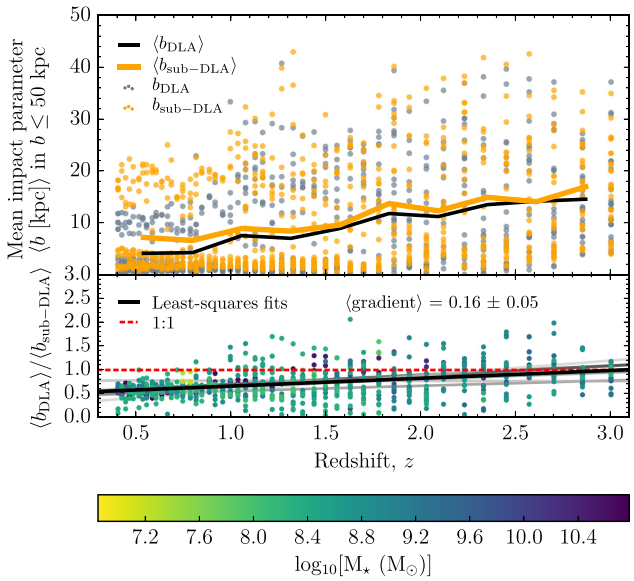

Figure 4. Angle-averaged mean impact parameters (b [kpc]) of sub-DLA and DLA sight-lines in seven haloes followed in our simulations. Top panel: Mean impact parameter of DLA (grey) and sub-DLA (orange) LOS of individual snapshots. Binned mean trends for DLA and sub-DLAs impact parameters as a function of redshift are depicted as solid lines following the same colour-coding. Bottom panel: Data represent the mean DLA to sub-DLA impact parameter ratio for each snapshot and from each side of the simulation box, colour-coded to stellar mass. The dashed red line marks a one to one ratio. Solid grey lines show fits to separate haloes. The solid black line depicts the mean relation.

eter evolution, we proceed to ask whether it is driven by a particular halo.

We find consistent correlation coefficients of the same magnitude using both the Pearson and the Spearman test (six positive and one negative correlation) for the individual haloes. The magnitude of these coefficients for individual haloes are similar to that of the population as a whole, but at elevated p-values in a broad range $\sim[10^{-33}\colon 10^{-1}]$. We therefore proceed to explicitly calculate linear fits to individual haloes (Fig. 4, grey lines). These fits yield similar gradients that systematically favour an evolution in the mean impact parameter ratio with time. With a fit to all data, we find a mean gradient of 0.16 ± 0.05 per unit redshift, i.e. at a formal 3.2σ significance (Fig. 4, black solid line).

This mean evolution in the ratio $\langle b_{\rm DLA}\rangle/\langle b_{\rm sub\text{-}DLA}\rangle$ with redshift is remarkably consistent with the analysis presented in Section 3.1. At $z \sim 3$ the ratio intercepts the 1:1 correlation. This is in part caused by the presence of multiple galaxies within the 50 kpc projected radius beam – each one generating its own internal distribution of DLA and sub-DLA LOSs – which on average will tend to average out any difference between the mean impact parameters discovered in the beam. In part, it is caused by the interaction between galaxies in the beam, which causes irregular gas flows that inhibit the formation of coherent structures, rendering a stochastic distribution. Moving down in redshift, the distribution of sub-DLA and DLA LOS diverge such that, on average, they are separated by a factor of two below redshifts $z \sim 0.5$.

It is striking that such a factor of $\sim$2 difference in mean projected separation between sub-DLA and DLA LOS is retrieved in observations at redshifts $z < 1.0$ (Rao et al. 2011; Rhodin et al. 2018). Indeed, even the absolute mean impact parameters derived in these studies ($\langle b\rangle^{\rm empirical}_{\rm DLA} \sim 15$ kpc, $\langle b\rangle^{\rm empirical}_{\rm sub-DLA} \sim 30$ kpc) are marginally consistent with some of the high means retrieved for individual galaxies in our simulations at comparable redshifts (see Fig. 4, top panel). As per Section 3.1 and Fig. 2 bottom row, however, we find significant detection fractions of both sub-DLA and DLA LOS to projected separations $\sim$50 kpc at all redshifts, and marginal inconsistencies in the absolute mean values between simulations and observations may reflect (observational) low number statistics and that cosmological zoom simulations have not converged on the spatial scales required to resolve cold gas in the CGM (Hummels et al. 2018; McCourt et al. 2018). We also note that Rahmati & Schaye (2014, R14) identify an anticorrelation between median impact parameter and $N_{\rm HI}$, for which they report $\langle b\rangle^{\rm R14}_{\rm sub-DLA} \sim 7$ pkpc and $\langle b\rangle^{\rm R14}_{\rm DLA} \sim 2$ pkpc. Albeit a large intrinsic scatter in the data, with 15–85 per cent percentiles which we estimate to extend from $2-29$ kpc and $0.5-4$ kpc for sub-DLAs and DLAs, respectively (Rahmati & Schaye 2014, private communication), their median values are significantly lower than those identified in observations and in our simulations. Additionally, despite a consistent factor of two difference in the means, their analysis is based on redshift $z = 3$, whereas our analysis of the redshift evolution suggests that such a clear separation is only in place at $z \lesssim 0.7$.

3.4 Do sub-DLA and DLA sightlines probe galaxies of different mass?

An alternative explanation to the idea that sub-DLA and DLA LOS trace different relations within a galaxy, is that they on average probe intrinsically different galaxy populations; sub-DLA LOS on average probing more massive galaxies than do DLA LOS (e.g. Khare et al. 2007; Kulkarni et al. 2010). Similar conclusions were also reached with deep ground-based imaging of sub-DLA hosts, which suggest that these systems preferentially sample more luminous – and therefore more massive galaxies than DLAs (Meiring et al. 2011). By measuring the stellar mass of the absorbing galaxies from matching spectral energy distribution galaxy templates to photometry, Augustin et al. (2018) and Rhodin et al. (2018) directly confirmed the apparent anticorrelation between the host's stellar mass and the H I column-density of the absorber.

If real, this correlation is remarkable as we expect both high- and low column-density LOS to pass through a given galaxy. In addition, the shape of the column-density frequency distribution function ($f(N_{\rm HI}, X)$) forces the frequency of sub-DLAs to outnumber that of DLAs. From Prochaska et al. (2014, P14) and with integration limits $[19.00, 20.30]_{\rm sub\text{-}DLA}$ and $[20.30, 25.00]_{\rm DLA}$, one finds $N_{\rm DLA}/N_{\rm sub\text{-}DLA} \sim 0.38$, which together with the apparent correlation described above implies an excess of massive gas-rich galaxies relative to low-mass galaxies, at odds with naive expectations from galaxy luminosity functions. A viable alternative is that the correlation is driven by sample selection effects.

Indeed Dessauges-Zavadsky, Ellison & Murphy (2009) argue for a metallicity bias at low-redshifts, while at $z > 1.7$ DLA and sub-DLA selections show statistically consistent metallicity distributions. Recent work on dust attenuation and quasar surveys confirms that we expect a dust-bias to preferentially act on high $N_{\rm HI}$, massive, metal-rich, dusty galaxies selected against quasar LOS (Vladilo & Péroux 2005; Fynbo et al. 2013a; Zafar & Watson 2013; Krogager et al. 2015; Noterdaeme, Petitjean & Srianand 2015; Zafar et al. 2015; Krogager et al. 2016; Fynbo et al. 2017). In Rhodin et al. (2018) we argue that the detection void in the low mass, low H I column-density parameter space could be explained

Downloaded from https://academic.oup.com/mnras/article-abstract/488/3/3634/5509589 by DTU Library - Technical Information Center of Denmark user on 16 September 2019

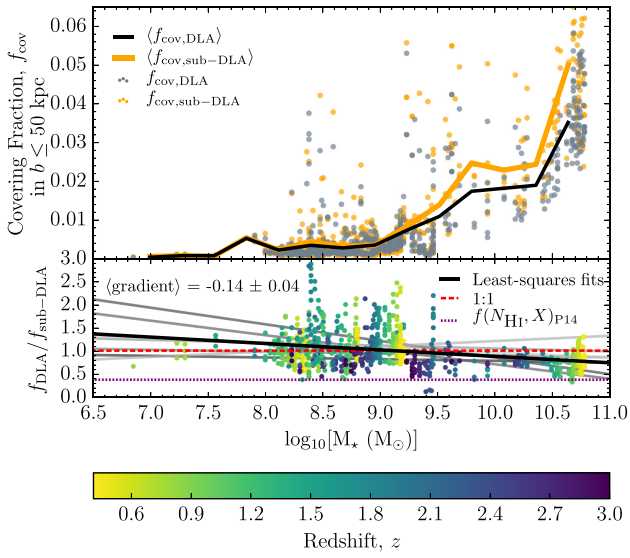

Figure 5. Same as Fig. 4, but for covering-fractions (f_{cov}) of sub-DLA and DLA LOS as a function of stellar mass. The bottom panel additionally includes the expected cosmological ratio of the number of DLAs to sub-DLAs, based on the P14 column-density distribution function (dotted purple line, see the text for more details).

by a functional dependence of the ratio in covering fraction of sub-DLA to DLA LOS with stellar mass, such that sub-DLAs are preferentially detected in more massive galaxies.

To test this prediction, we calculate the covering fraction (f_{cov}) of sub-DLA and DLA LOSs in each halo, and repeat the statistical analysis described in Section 3.3. Utilizing the column-density maps created with equation (3), we define f_{cov} as the fractional area with column densities above the (sub-)DLA limit in a circular beam with 50 kpc galactocentric projected separation. We present the angle-averaged results in Fig. 5. In the top panel, we plot the data for individual galaxies f_{cov} in DLA (grey) and sub-DLA (orange) LOS, together with binned-mean relations in the respective colours, as a function of stellar mass. f_{cov} for sub-DLA and DLA LOS correlate with stellar mass such that larger stellar masses, on average, are associated with larger f_{cov}. At stellar mass $\log_{10}[M_\star\ (M_\odot)] \sim 10$ the entire central region sees an increase in neutral gas, which leads to a rapid increase in the final covering fractions. For the most massive disc galaxy in our sample, this increase correlates with rapid disc growth at $z \sim 1.5$. This increase in gas disc sizes of galaxies forming in Milky-Way-mass haloes, around this redshift and stellar mass, is found in larger samples of zoom simulations (Kretschmer et al. in preparation), as well as observationally in terms of the stellar size–mass relation (see compilation by Agertz & Kravtsov 2015).

Calculating the Pearson correlation coefficient; the Spearman rank-order correlation coefficient, and their associated null-hypothesis's p-value, we find PC(z, $f_{DLA}/f_{sub\text{-}DLA}$) = [−0.162, $\sim 10^{-6}$] and SC(z, $f_{DLA}/f_{sub\text{-}DLA}$) = [−0.164, $\sim 10^{-6}$], whereas PC($\log_{10}[M_\star\ (M_\odot)]$, $f_{DLA}/f_{sub\text{-}DLA}$) = [−0.273, $\sim 10^{-15}$] and SC($\log_{10}[M_\star\ (M_\odot)]$, $f_{DLA}/f_{sub\text{-}DLA}$) = [−0.244, $\sim 10^{-12}$]. With consistent results, we conclude that a correlation in differential covering fraction with stellar mass indeed dominates over a correlation with redshift by a factor of ∼2. In Fig. 5 lower panel, we show the ratio of DLA to sub-DLA covering fractions to envisage the differential scaling with stellar mass, and colour-code the data by redshift.

Having established the subordinate role of redshift to stellar mass in the covering fraction ratio, we proceed to ask whether the correlation is driven by a particular halo. Individual haloes display similar correlation coefficients to that of the population as a whole, but at elevated p-values in the range $\sim[10^{-3}: 10^{-1}]$, suggesting that each halo contributes to the final p-value and correlation-strength of the population. We therefore proceed to calculate linear fits to the data of individual haloes (overplotted as grey lines). With consistent trends, we find a mean differential covering fraction ratio per unit logarithmic stellar mass of -0.14 ± 0.04. This corresponds to a weak functional dependence at a 3.5σ significance which we overplot as a black solid line. Qualitatively, this correlation with stellar mass is consistent with the results of Faucher-Giguère et al. (2015) who report that the covering fraction of gas at different column-density thresholds is sensitive to individual dark matter halo masses for LBGs at $z \sim 2$.

Despite weak, if real and acting across the three decades in stellar mass ($\sim 8.0 < \log_{10}[M_\star\ (M_\odot)] < 11.$) identified in observations, we expect this gradient to account for $3 \times 0.14 \sim 0.4$, i.e. a 40 per cent measured effect. We consider a more realistic value to be that produced within the 1σ dispersion in the stellar mass distribution of confirmed hosts. For the sample used in Rhodin et al. (2018), with mean and dispersion in stellar mass of 9.87 ± 0.66, we expect a measured effect of ∼20 per cent. Whereas we expect this effect to contribute to the observed anticorrelation, a direct comparison to the current set of data is beyond the scope of this work, as such a comparison has to account for sample selection functions and observational strategy bias.

As a reference-point, we instead calculate the predicted ratio of the number of DLAs to sub-DLAs, based on $f(N_{HI}, X)$. With the P14 parametrization, $f(N_{HI}, X)_{P14}$, we expect a ratio $N_{DLA}/N_{sub\text{-}DLA} = 0.38$. We overplot this estimator as a dotted purple line. Using the $f(N)$ statistic as an unbiased proxy for the cosmic average covering fraction ratio in DLAs to sub-DLAs, we find an overdensity of DLA (or equivalently, an underdensity of sub-DLA) LOS within a 50 kpc projected radius beam from the mass centre of the hosting halo. From this, we conclude that the majority of sub-DLAs are located at separations $b > 50$ kpc.

4 CONCLUSIONS

In this work, we have used a cosmological zoom-in hydrodynamics simulation of the assembly of a Milky-Way-mass galaxy to study beams of 50 kpc radius centred on galaxies to study the environments capable of producing sub-DLA and DLA LOS. Building probability functions of observables and logging their redshift evolution, we have matched these to the most up-to-date compilation of spectroscopically confirmed absorbing galaxies (Christensen et al. 2019; Møller & Christensen 2019), and to analytic models (Fynbo et al. 2008; Krogager et al. 2017). The main results can be summarized as follows:

(i) Recent advances have shown that increased numerical resolution leads to increased long-lived cool gas content on progressively smaller size scales (Hummels et al. 2018); a doubling in covering fraction of Lyman limit systems within 150 kpc (van de Voort et al. 2019); and an improved match to observed kinematic structures of absorbing gas (Peeples et al. 2019). Our results are in qualitative agreement, suggesting that increased numerical resolution leads to an excess of H I coverage in galaxy haloes and the CGM. This increases the mean impact parameters of strong H I absorbers and produces detection probabilities at all observed values.

(ii) High numerical resolution and an effective feedback prescription allow us to reproduce the column density distribution function

Downloaded from https://academic.oup.com/mnras/article-abstract/488/3/3634/5509589 by DTU Library - Technical Information Center of Denmark user on 16 September 2019

of blind quasar surveys and for individual galaxies. This validates the application of these simulations to study sub-DLA and DLAs in a galactic context.

(iii) At redshift $z \lesssim 1$ we statistically match the distribution of impact parameters with metallicity based on the analytical F08 + K17 model for DLAs. For higher redshifts, and when including the contribution from sub-DLAs, we find a greater statistical missmatch and excess detection probability beyond the envelope of the analytical model.

(iv) To understand the physical origin of the detection-fractions, we perform a disc–halo separation using the baryonic angular momentum vector and the density profile of neutral gas. We find that ∼80 per cent of DLAs originate in extended H I discs, with the remaining 20 per cent originating in the halo. Including sub-DLAs increases the relative contribution of the halo to 40 per cent. We note that this separation relies on the existence of a clearly defined H I disc, and our results are limited to redshifts $z < 1$.

(v) We find a 3.2σ significance redshift evolution in the mean impact parameters of sub-DLA and DLA LOS. At high redshifts the mean impact parameters overlap, but separate at successively lower redshifts with sub-DLA LOS on average identified at a factor two larger projected separations than DLAs at $z \sim 0.4$. At all redshifts, our simulations can match the observational data.

(vi) We find a 3.5σ significance anticorrelation in differential covering-fraction of DLA to sub-DLA LOSs with stellar mass. This suggests an observational selection effect that causes the preferential detection of sub-DLAs in more massive galaxies in the low-redshift Universe.

Despite the remarkable agreement with observations – which may suggest that strong H I absorption predominantly forms in typical gas-rich disc galaxies – we caution against overinterpreting the results. Whereas our simulation qualitatively capture and explain the current set of observations, the results should be anchored in the next-generation of zoom-in simulations performed across a large grid to account for environmental dependence and sample the underlying dark matter halo distribution.

ACKNOWLEDGEMENTS

We thank the referee for valuable comments which greatly improved the scientific content, language, and clarity of the work presented here. N. H. P. Rhodin and L. Christensen acknowledge support by the Independent Research Fund Denmark (DFF), grant number DFF-4090-00079. J. P. U. Fynbo and the Cosmic Dawn Center are funded by the Danish National Research Foundation (DNRF). This work used the COSMA Data Centric system at Durham University, operated by the Institute for Computational Cosmology on behalf of the Science and Technology Facilities Council (STFC) DiRAC High Performance Computing (HPC) Facility (www.dirac.ac.uk). This equipment was funded by a Department for Business, Innovation and Skills (BIS) National E-infrastructure capital grant ST/K00042X/1, DiRAC Operations grant ST/K003267/1, and Durham University. DiRAC is part of the National E-Infrastructure. O. Agertz acknowledges support from the Swedish Research Council, grant number 2014- 5791. O. Agertz and F. Renaud acknowledge support from the Knut and Alice Wallenberg Foundation.

REFERENCES

Agertz O., Kravtsov A. V., 2015, ApJ, 804, 18
Agertz O., Kravtsov A. V., 2016, ApJ, 824, 79
Agertz O., Teyssier R., Moore B., 2009, MNRAS, 397, L64
Agertz O., Kravtsov A. V., Leitner S. N., Gnedin N. Y., 2013, ApJ, 770, 25
Altay G., Theuns T., Schaye J., Crighton N. H. M., Dalla Vecchia C., 2011, ApJ, 737, L37
Altay G., Theuns T., Schaye J., Booth C. M. Dalla Vecchia C. , 2013, MNRAS, 436, 2689
Asplund M., Grevesse N., Sauval A. J., Scott P., 2009, ARA&A, 47, 481
Aubert D., Teyssier R., 2010, ApJ, 724, 244
Augustin R. et al., 2018, MNRAS, 478, 3120
Bird S., Vogelsberger M., Haehnelt M., Sijacki D., Genel S., Torrey P., Springel V., Hernquist L., 2014, MNRAS, 445, 2313
Bird S., Haehnelt M., Neeleman M., Genel S., Vogelsberger M., Hernquist L., 2015, MNRAS, 447, 1834
Blondin J. M., Wright E. B., Borkowski K. J., Reynolds S. P., 1998, ApJ, 500, 342
Boissier S., Prantzos N., 2001, MNRAS, 325, 321
Cadiou C., Dubois Y., Pichon C., 2019, A&A, 621, A96
Cen R., 2012, ApJ, 748, 121
Chabrier G., 2003, PASP, 115, 763
Christensen L., Wisotzki L., Roth M. M., Sánchez S. F., Kelz A., Jahnke K., 2007, A&A, 468, 587
Christensen L., Møller P., Rhodin N. H. P., Heintz K. E., Fynbo J. P. U., 2019, MNRAS, in press
Cioffi D. F., McKee C. F., Bertschinger E., 1988, ApJ, 334, 252
Dessauges-Zavadsky M., Ellison S. L., Murphy M. T., 2009, MNRAS, 396, L61
Eisenstein D. J., Hut P., 1998, ApJ, 498, 137
Erkal D., Gnedin N. Y., Kravtsov A. V., 2012, ApJ, 761, 54
Faucher-Giguère C.-A., Hopkins P. F., Kereš D., Muratov A. L., Quataert E., Murray N., 2015, MNRAS, 449, 987
Fumagalli M., Prochaska J. X., Kasen D., Dekel A., Ceverino D., Primack J. R., 2011, MNRAS, 418, 1796
Fynbo J. P. U., Prochaska J. X., Sommer-Larsen J., Dessauges-Zavadsky M., Møller P., 2008, ApJ, 683, 321
Fynbo J. P. U. et al., 2010, MNRAS, 408, 2128
Fynbo J. P. U. et al., 2011, MNRAS, 413, 2481
Fynbo J. P. U., Krogager J.-K., Venemans B., Noterdaeme P., Vestergaard M., Møller P., Ledoux C., Geier S., 2013a, ApJS, 204, 6
Fynbo J. P. U. et al., 2013b, MNRAS, 436, 361
Fynbo J. P. U. et al., 2017, A&A, 606, A13
Genel S., Vogelsberger M., Nelson D., Sijacki D., Springel V., Hernquist L., 2013, MNRAS, 435, 1426
Haardt F., Madau P., 1996, ApJ, 461, 20
Haehnelt M. G., Steinmetz M., Rauch M., 1998, ApJ, 495, 647
Hahn O., Abel T., 2011, MNRAS, 415, 2101
Holmberg E., 1975, in Sandage A., Sandage M., Kristian J., eds, Galaxies and the Universe. University of Chicago Press, Chicago, p. 123
Hopkins P. F., Kereš D., Oñorbe J., Faucher-Giguère C.-A., Quataert E., Murray N., Bullock J. S., 2014, MNRAS, 445, 581
Hummels C. B. et al., 2018, preprint (arXiv:1811.12410)
Khare P., Kulkarni V. P., Péroux C., York D. G., Lauroesch J. T., Meiring J. D., 2007, A&A, 464, 487
Kim J.-h. et al., 2014, ApJS, 210, 14
Kim J.-h. et al., 2016, ApJ, 833, 202
Kim C.-G., Ostriker E. C., 2015, ApJ, 802, 99
Krogager J.-K., Fynbo J. P. U., Møller P., Ledoux C., Noterdaeme P., Christensen L., Milvang-Jensen B., Sparre M., 2012, MNRAS, 424, L1
Krogager J.-K. et al., 2013, MNRAS, 433, 3091
Krogager J.-K. et al., 2015, ApJS, 217, 5
Krogager J.-K. et al., 2016, ApJ, 832, 49
Krogager J.-K., Møller P., Fynbo J. P. U., Noterdaeme P., 2017, MNRAS, 469, 2959
Krumholz M. R., McKee C. F., Tumlinson J., 2008, ApJ, 689, 865
Krumholz M. R., McKee C. F., Tumlinson J., 2009, ApJ, 693, 216
Kulkarni V. P., Khare P., Som D., Meiring J., York D. G., Péroux C., Lauroesch J. T., 2010, New Astron., 15, 735

Downloaded from https://academic.oup.com/mnras/article-abstract/488/3/3634/5509589 by DTU Library - Technical Information Center of Denmark user on 16 September 2019

Ledoux C., Petitjean P., Fynbo J. P. U., Møller P., Srianand R., 2006, A&A, 457, 71
Leitherer C. et al., 1999, ApJS, 123, 3
Liang C. J., Kravtsov A. V., Agertz O., 2016, MNRAS, 458, 1164
Liang C. J., Kravtsov A. V., Agertz O., 2018, MNRAS, 479, 1822
Martizzi D., Faucher-Giguère C.-A., Quataert E., 2015, MNRAS, 450, 504
McCourt M., Oh S. P., O'Leary R., Madigan A.-M., 2018, MNRAS, 473, 5407
Meiring J. D., Lauroesch J. T., Haberzettl L., Kulkarni V. P., Péroux C., Khare P., York D. G., 2011, MNRAS, 410, 2516
Monier E. M., Turnshek D. A., Rao S., 2009, MNRAS, 397, 943
Mo H. J., Mao S., White S. D. M., 1998, MNRAS, 295, 319
Møller P., Warren S. J., 1998, MNRAS, 299, 661
Møller P., Fynbo J. P. U., Ledoux C., Nilsson K. K., 2013, MNRAS, 430, 2680
Møller P., Christensen L., 2019, MNRAS, in press
Nagamine K., Wolfe A. M., Hernquist L., Springel V., 2007, ApJ, 660, 945
Neeleman M., Wolfe A. M., Prochaska J. X., Rafelski M., 2013, ApJ, 769, 54
Noterdaeme P., Petitjean P., Ledoux C., Srianand R., 2009, A&A, 505, 1087
Noterdaeme P. et al., 2012, A&A, 547, L1
Noterdaeme P., Petitjean P., Srianand R., 2015, A&A, 578, L5
Padoan P., Haugbølle T., Nordlund Å., 2012, ApJ, 759, L27
Peeples M. S. et al., 2019, ApJ, 873, 129
Péroux C., Dessauges-Zavadsky M., D'Odorico S., Kim T.-S., McMahon R. G., 2003, MNRAS, 345, 480
Péroux C., Bouché N., Kulkarni V. P., York D. G., Vladilo G., 2012, MNRAS, 419, 3060
Peterson B. M., Strom S. E., Strom K. M., 1979, AJ, 84, 735
Pettini M., Shapley A. E., Steidel C. C., Cuby J.-G., Dickinson M., Moorwood A. F. M., Adelberger K. L., Giavalisco M., 2001, ApJ, 554, 981
Pontzen A. et al., 2008, MNRAS, 390, 1349
Power C., Navarro J. F., Jenkins A., Frenk C. S., White S. D. M., Springel V., Stadel J., Quinn T., 2003, MNRAS, 338, 14
Prochaska J. X., Wolfe A. M., 1997, ApJ, 487, 73
Prochaska J. X., Gawiser E., Wolfe A. M., Castro S., Djorgovski S. G., 2003, ApJ, 595, L9
Prochaska J. X., Herbert-Fort S., Wolfe A. M., 2005, ApJ, 635, 123
Prochaska J. X., Madau P., O'Meara J. M., Fumagalli M., 2014, MNRAS, 438, 476
Rafelski M., Neeleman M., Fumagalli M., Wolfe A. M., Prochaska J. X., 2014, ApJ, 782, L29
Rahmani H. et al., 2016, MNRAS, 463, 980
Rahmati A., Schaye J., 2014, MNRAS, 438, 529
Rahmati A., Pawlik A. H., Raičević M., Schaye J., 2013, MNRAS, 430, 2427
Raiteri C. M., Villata M., Navarro J. F., 1996, A&A, 315, 105
Rao S. M., Belfort-Mihalyi M., Turnshek D. A., Monier E. M., Nestor D. B., Quider A., 2011, MNRAS, 416, 1215
Reddy N. A., Steidel C. C., 2009, ApJ, 692, 778
Reddy N. A., Steidel C. C., Pettini M., Adelberger K. L., Shapley A. E., Erb D. K., Dickinson M., 2008, ApJS, 175, 48
Rhodin N. H. P., Christensen L., Møller P., Zafar T., Fynbo J. P. U., 2018, A&A, 618, A129
Romeo A. B., Agertz O., Moore B., Stadel J., 2008, ApJ, 686, 1
Rosen A., Bregman J. N., 1995, ApJ, 440, 634
Schaye J. et al., 2015, MNRAS, 446, 521
Som D., Kulkarni V. P., Meiring J., York D. G., Péroux C., Lauroesch J. T., Aller M. C., Khare P., 2015, ApJ, 806, 25
Sutherland R. S., Dopita M. A., 1993, ApJS, 88, 253
Teyssier R., 2002, A&A, 385, 337
Thornton K., Gaudlitz M., Janka H.-T., Steinmetz M., 1998, ApJ, 500, 95
Tytler D., 1982, Nature, 298, 427
van de Voort F., Springel V., Mandelker N., van den Bosch F. C., Pakmor R., 2019, MNRAS, 482, L85
Vladilo G., Péroux C., 2005, A&A, 444, 461
Vogelsberger M. et al., 2014, MNRAS, 444, 1518
Wetzel A. R., Hopkins P. F., Kim J.-. hoon ., Faucher-Giguère C.-A., Kereš D., Quataert E., 2016, ApJ, 827, L23
Wise J. H., Abel T., Turk M. J., Norman M. L., Smith B. D., 2012, MNRAS, 427, 311
Wolfe A. M., Turnshek D. A., Smith H. E., Cohen R. D., 1986, ApJS, 61, 249
Zafar T., Watson D., 2013, A&A, 560, A26
Zafar T., Popping A., Péroux C., 2013, A&A, 556, A140
Zafar T. et al., 2015, A&A, 584, A100
Zwaan M. A., van der Hulst J. M., Briggs F. H., Verheijen M. A. W., Ryan-Weber E. V., 2005, MNRAS, 364, 1467

This paper has been typeset from a TEX/LATEX file prepared by the author.

Downloaded from https://academic.oup.com/mnras/article-abstract/488/3/3634/5509589 by DTU Library - Technical Information Center of Denmark user on 16 September 2019